Cell Reports
Physical Science

CellPress
OPEN ACCESS

Article

Boosting areal capacitance in WO_3-based supercapacitor materials by stacking nanoporous composite films

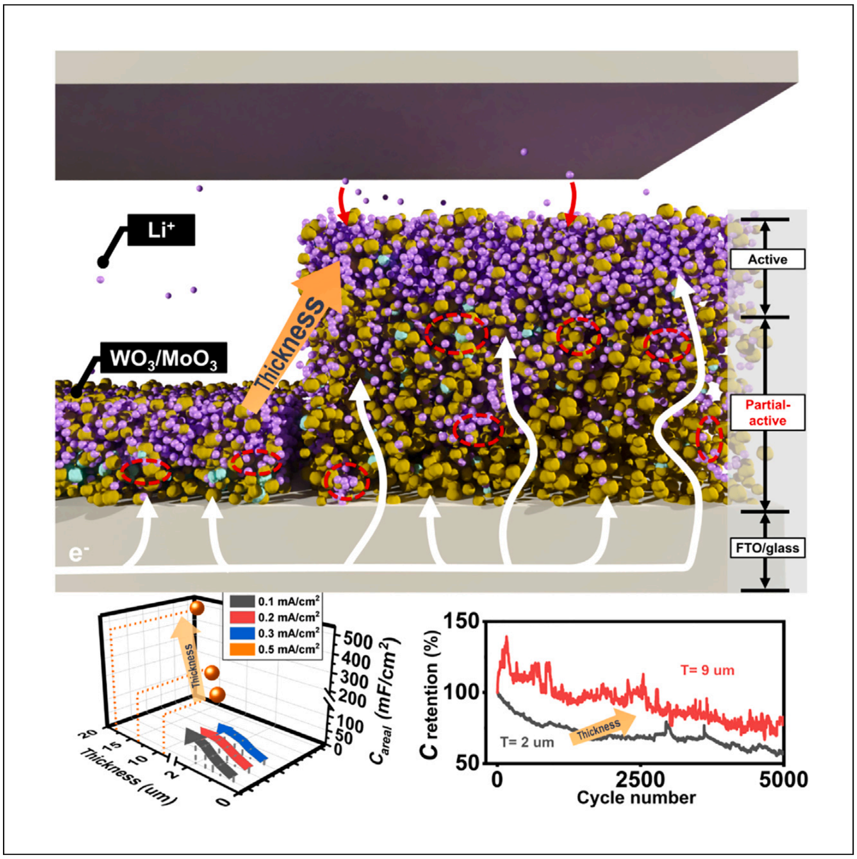

Wei et al. develop electroexploding wire and spray-coating techniques to prepare nanoporous WO_3/MoO_3 composite films. This work demonstrates both supercapacitive energy storage and methods to boost energy storage capabilities through the stacking of the nanoporous films.

Chia-Chun Wei, Po-Hung Lin, Chin-En Hsu, ..., Akhil Pradiprao Khedulkar, Ruey-An Doong, Kazuhito Tsukagoshi

wbjian@nycu.edu.tw

Highlights

Green technologies are demonstrated for the preparation of energy storage devices

Li-ion diffusion coefficient of 1.12×10^{-7} cm^2/s in WO_3-based systems

Areal capacitance up to 496 mF/cm^2 is demonstrated

Tradeoff between areal and gravimetric capacitances is explored

Wei et al., Cell Reports Physical Science 5, 101836
March 20, 2024 © 2024 The Author(s).
https://doi.org/10.1016/j.xcrp.2024.101836

Cell Reports
Physical Science

CellPress
OPEN ACCESS

Article

Boosting areal capacitance in WO_3-based supercapacitor materials by stacking nanoporous composite films

Chia-Chun Wei,[1] Po-Hung Lin,[1] Chin-En Hsu,[1] Wen-Bin Jian,[1,7,*] Yu-Liang Lin,[2] Jiun-Tai Chen,[2] Soumallya Banerjee,[3,4] Chih-Wei Chu,[4] Akhil Pradiprao Khedulkar,[1] Ruey-An Doong,[5] and Kazuhito Tsukagoshi[1,6]

SUMMARY

High-capacity energy storage devices are of interest in various applications, but are not always easy to scale up, and they may experience tradeoffs between areal and gravimetric capacitance. Here, nanoporous WO_3/MoO_3 films are prepared using electroexploding wire and spray-coating techniques for the exploration of the tradeoffs between areal and gravimetric capacitance. The nanoporous films are extended through nanoparticle stacking, which is accompanied by increasing thickness. The diffusion coefficient measured with cyclic voltammetry increases exponentially with thickness and reaches 1.12×10^{-7} cm^2/s for Li-ion intercalations. In galvanostatic charge-discharge curves, the highest areal capacitance of 496 mF/cm^2 is obtained at 0.5 mA/cm^2 for an 18-μm-thick film, and the gravimetric capacitance is 95.2 F/g at 0.13 A/g for a 1.6-μm-thick film. The film thickness is adjusted to optimize either areal or gravimetric capacitances, and high retention abilities imply the possibility of application in high-performance supercapacitive applications.

INTRODUCTION

The huge consumption of fossil fuel energy has led to energy crises, CO_2 emissions, and climate change. The building, industry, and transport sectors have dominated among all global energy consumption.[1] In addition, the building sector has consumed approximately one-third of global energy and generated one-fourth of the CO_2 emissions.[1] To contain the CO_2 emissions and prevent an energy crisis, sustainable and renewable energy resources with energy storage systems must be developed.[2] As for the transport sector and vehicles, they are under transition to electrification, and, consequently, energy storage systems have played the most important role.[3] The continued development of energy storage systems will facilitate the prevention of climate change and energy crises, and it has accelerated the applications of electric vehicles and portable electronics. One example is the potential to save energy using smart windows based on electrochromic (EC) materials[4–6] that can reduce energy consumption and CO_2 emissions as well. Those EC materials were implemented for the development of supercapacitors[7] as well as EC energy storage devices (ESDs).[5]

The energy storage system manifested itself in the significant application of green energy and electric vehicles. There were several different types of energy storage systems. The most well-established electrochemical energy storage systems were

[1]Department of Electrophysics, National Yang Ming Chiao Tung University, 1001 University Road, Hsinchu 300093, Taiwan

[2]Department of Applied Chemistry, National Yang Ming Chiao Tung University, 1001 University Road, Hsinchu 300093, Taiwan

[3]Department of Material Science and Engineering, National Yang Ming Chiao Tung University, 1001 University Road, Hsinchu 300093, Taiwan

[4]Research Center for Applied Sciences, Academia Sinica, No. 128, Sec. 2, Academia Road, Taipei 11529, Taiwan

[5]Institute of Analytical and Environmental Sciences, National Tsing Hua University, Hsinchu 300044, Taiwan

[6]International Center for Materials Nanoarchitectonics (WPI-MANA), National Institute for Materials Science (NIMS), Tsukuba, Ibaraki 305-0044, Japan

[7]Lead contact

*Correspondence: wbjian@nycu.edu.tw

https://doi.org/10.1016/j.xcrp.2024.101836

Pb batteries, which still possessed the world's largest market and underwent steady innovation in the design of their working electrodes with a high recycling rate.[8] In addition, the technology of Li-ion batteries developed and evolved rapidly in the past 3 decades due to specific features of high energy densities, low self-discharge properties, high open-circuit voltage, and long lifespan.[9] The Li-ion batteries were based on the mechanisms of Li-ion intercalation and deintercalation. However, there was another type of energy storage system, the supercapacitor, that implemented the mechanisms of ion adsorptions and surface redox reactions.[2,7] When high-power charging or discharging was required, supercapacitors could either replace or complement other types of batteries. Supercapacitors, also known as ultracapacitors or electrochemical capacitors, consisted of two kinds of charge storage mechanisms. The first kind of charge storage mechanisms was the electrochemical double-layer capacitor (EDLC) that signified the adhesion of electrolyte ions on the surface of charged electrodes to form the electric double layer with a nanoscale separation gap.[10,11] This mechanism existed in carbon-decorated electrodes and required highly porous structures, and it exhibited a high-power density and remarkable cycling reversibility. The second kind of charge storage mechanism was the pseudocapacitor, which indicated the faradic reaction of oxidations and reductions between the electrolytes and electrodes.[2,7] Although the cycling reversibility and the power density were not comparable to the EDLC, the pseudocapacitor revealed other benefits of high specific capacitances and energy densities. In the past 2 decades, syntheses of nanomaterials progressed rapidly[12,13] and facilitated the advances of supercapacitors.[2] To integrate the advantages of the EDLC and the pseudocapacitor, asymmetric supercapacitor cells were proposed to decorate either one or both positive and negative electrodes.[14]

Hydrous ruthenium oxides (RuO_2) were discovered to be excellent pseudocapacitor materials that exhibited a high weight capacitance of up to 800 F/g,[15] whereas such noble metal oxide materials posed an intrinsic, noneconomic drawback and a severe problem in mass production. Abundant metal oxides such as Fe_3O_4 and MnO_2 were proposed and used alternatively for supercapacitors. For example, the gravimetric capacitance of carbon-MnO_2 was estimated to be $\sim$20 F/g.[16] In recent years, WO_3 manifested itself as a high potential material for EC applications,[4–7] and its hybrid composites had been demonstrated to be energy storage smart windows.[17] With the advances in nanotechnology, the bulk WO_3 had been converted to nanomaterials, giving a high surface-to-volume ratio and enhancing the supercapacitive property.[18–21] Those nanostructured WO_3s almost presented a high specific capacitance of $\sim$400 F/g at 1 A/g,[19] which was comparable to that of RuO_2 supercapacitors. In addition to pure, nanostructured WO_3, there were reports of hybridized composites and asymmetric supercapacitors based on WO_3 using several chemical or physical synthesis methods. For instance, an electrochemical co-deposition method was used to prepare WO_3-V_2O_5 composites for supercapacitive applications that exhibited an areal capacitance (C_{areal}) of $\sim$40 mF/cm^2 at 0.5 mA/cm^2.[22] However, hydrothermal synthesis and electrochemical polymerization were used to prepare honeycombed porous P5FIn/WO_3 nanocomposites for supercapacitors, revealing an area capacitance of $\sim$34 mF/cm^2 at 0.1 mA/cm^2.[23] All of these studies pointed to the importance of preparing WO_3-based porous materials. In addition, the areal capacitance normally increased with an increase in the thickness of metal-oxide materials, and the conductivity at outer surface and the probability of ion diffusing deeply into metal-oxide films brought about the poor performance of energy storage. In all of these issues, the porosity of metal oxides was demonstrated to exhibit an essential role in enhancing energy storage.[24,25]

In previous studies, we developed a scaling-up method to prepare nanoparticulate films of WO_3 and MoO_3 composites using the green technologies of electroexploding wire and spray-coating techniques.[5] We discovered that $(WO_3)_{87.5}(MoO_3)_{12.5}$ composite films exposed optimum EC properties, such as high charge density, coloration efficiency, and transmittance variation. In the present work, we explore deeply into energy storage capabilities for the same nanoparticulate $(WO_3)_{87.5}(MoO_3)_{12.5}$ composite films, presenting a potential application as supercapacitor electrodes. The intrinsic properties of the nanoparticulate films, including the nanoporosity and stackability feature, are implemented for the development of high supercapacitive performances that have rarely been explored. Currently, most of the high-capacitance supercapacitors based on WO_3 are fabricated on carbon-based substrate such as carbon fabric and graphenes,[26,27] which may lead to misinterpretations of contributions from either intrinsic WO_3- or carbon-based material.[28] The nanoporous $(WO_3)_{1-x}(MoO_3)_x$ composite film manifests itself as an easy scaling-up structure on both sizes and areal capacities for supercapacitive applications. The present study paves the way for developing high capacity on EC ESDs.

RESULTS AND DISCUSSION

Characterization of WO_3 and MoO_3 nanoparticles (NPs)

WO_3 and MoO_3 NPs were synthesized using the electroexploding wire technique and mixed in solution. The transmission electron microscopy (TEM) images of the two species are displayed in Figure S1A. For a detailed inspection, a high-resolution TEM image of WO_3 is offered in Figure S1B, presenting an interplanar spacing of ~0.38 nm for the (021) plane of monoclinic WO_3.[6] Accordingly, interplanar spacings of ~0.18 and ~0.25 nm in Figure S1C are assigned to the (230) and (041) planes of orthorhombic MoO_3. Further investigation of NPs, including size distributions, X-ray diffraction (XRD) analyses, and Raman spectroscopy analyses, were reported previously.[5]

Characterization of WO_3/MoO_3 composite films

In this study, we adopt nanoparticulate $(WO_3)_{87.5}(MoO_3)_{12.5}$ films for the further exploration of supercapacitive and energy storage capabilities. Figure 1A presents a side view of a scanning electron microscopy (SEM) image for a $(WO_3)_{87.5}(MoO_3)_{12.5}$ film prepared with 5 mL of mixed WO_3 and MoO_3 NP suspensions. The molar number of the 5-mL suspension corresponds to ~5.2×10^{-6} mol (see the detailed calculations in the supplemental experimental procedures). The thickness of the as-prepared composite film is estimated to be ~500 nm, which is marked in Figure 1A. The thicknesses of the other nanoparticulate $(WO_3)_{87.5}(MoO_3)_{12.5}$ films prepared with volumes of 10, 15, 20, and 25 mL are measured in SEM images shown in Figures S2A—S2D. The thickness as a function of molar number of $(WO_3)_{87.5}(MoO_3)_{12.5}$ composites is displayed in the inset to Figure 1A. With the thickness of the composite films determined, the sample names are designated accordingly as presented in Table S1. The surface morphologies of $(WO_3)_{87.5}(MoO_3)_{12.5}$ composite films were examined using SEM. Figures S3A and S3C reveal the morphology of the as-prepared samples, whereas Figures S3B and S3D show the surface morphology after the electrochemical test, with Li ions intercalated. After performing electrochemical measurements and putting the film in the colored state, additional clusters (see Figure S3B) and, sometimes, microrods (Figure S3D), will be observed at the surface. These additional materials could be attributed to Li compounds when the carbonate-based electrolyte was used.[29,30] The elemental mappings of the side-view images of sample WMo-05 are provided in Figures S4A–S4C. It is observed that the W and Mo elements are uniformly distributed in the composite films. There are no aggregations in the simple mixing of NP suspensions for the preparation of

Please cite this article in press as: Wei et al., Boosting areal capacitance in WO_3-based supercapacitor materials by stacking nanoporous composite films, Cell Reports Physical Science (2024), https://doi.org/10.1016/j.xcrp.2024.101836

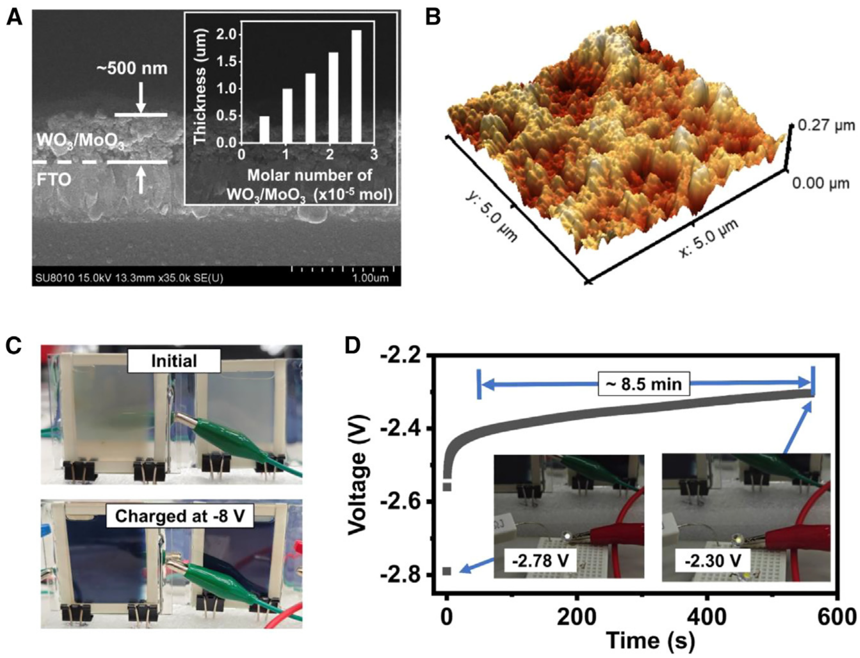

Figure 1. Morphology and energy storage performance

(A) Side-view SEM image of nanoparticulate WO_3/MoO_3 films of sample WMo-05, with a scale bar of 1 µm. The thickness of ~500 nm and the FTO substrate are marked on the SEM image. The thicknesses are estimated to be 489 ± 39, 1,000 ± 46, 1,280 ± 85, 1,670 ± 120, and 2,080 ± 160 nm for samples WMo-05, WMo-10, WMo-13, WMo-16, and WMo-20, respectively. The inset presents the thickness in micrometers of the nanoparticulate films as a function of the molar number of WO_3/MoO_3 composites.

(B) Top-view AFM image of sample WMo-05 in the 3-dimensional configuration. The root-mean-square roughness is ~42.2 nm within an area of 5 × 5 μm^2.

(C) An EC ESD in its initial (top) and charged (colored) (bottom) states. The EC ESD is based on sample WMo-20, with an active area of 3.5 × 4.0 cm^2 on 1 side of the FTO glass substrate. The charge storage system consists of 2 ESDs connected in series to offer sufficient voltage for driving LEDs.

(D) Discharging voltage as a function of time for the 2 ESDs connected with an LED. The discharging period lasts longer than 8.5 min while the discharging voltage changes from −2.78 to −2.30 V.

$(WO_3)_{87.5}(MoO_3)_{12.5}$ composite films. Moreover, Figure S5A offers Raman spectra of the $(WO_3)_{87.5}(MoO_3)_{12.5}$ composite films based on samples from WMo-05 to WMo-20. The spectra only display differences in intensity for different samples, whereas the characteristic peaks remain in the same position. The Raman spectrum of sample WMo-13 is magnified in Raman shifts ranging from 600 to 1,000 cm^{-1} and is presented in Figure S5B. The spectrum is fitted with several Gaussian peaks and separated into bands at Raman shifts of 670, 713, 807, 816, and 896 cm^{-1}. The Raman bands at 713 and 807 cm^{-1} indicate the monoclinic structure of WO_3 owing to the stretching vibrations of O–W–O bonds.[5,31,32] The bands at 670 and 816 cm^{-1} reveal the orthorhombic MoO_3, attributed to the stretching vibrations of the triply coordinated oxygen and the O=Mo and Mo–O–Mo bonds.[5,33] In addition, the band at 896 cm^{-1} denotes the monoclinic crystal phase of MoO_3.[5,33] In addition, XRD data in Figure S6 reveal similar profiles for samples of different film thicknesses. X-ray photoelectron spectroscopy (XPS) spectra for the surface electronic structure, presented in Figure S7, also provide consistent results among samples of different thicknesses. In Figure S8, the XPS spectra of W 4f, Mo 3d, and Li 1s core levels for sample WMo-20 are offered both before and after electrochemical testing. Accompanied by negligible chemical shifting of W 1s and Mo 3d, an additional band of Li 1s

Please cite this article in press as: Wei et al., Boosting areal capacitance in WO_3-based supercapacitor materials by stacking nanoporous composite films, Cell Reports Physical Science (2024), https://doi.org/10.1016/j.xcrp.2024.101836

with a weak intensity can be observed in the spectrum after electrochemical testing. This result demonstrates the presence of the Li compound at the surface that is illustrated in the SEM images in Figure S3.

The nanoparticulate films reveal intrinsic nanoporosity due to the stacking of different sizes of NPs. Figure 1B exhibits a top-view atomic force microscopy (AFM) image of sample WMo-05. Fruitful cavities of different sizes appear on the surface. In particular, the feature of nanoporosity benefits chemical or physical reactions on the surface and ion diffusions in cavities and channels. The mass of the $(WO_3)_{87.5}(MoO_3)_{12.5}$ composite films for sample WMo-05 is evaluated as being 1.1 mg (see descriptions in the supplemental experimental procedures). For those compact films prepared by either thermal evaporation or sputtering, such films shall possess a thickness of 296 nm, whereas the thickness of sample WMo-05 is ~500 nm—much higher than that of compact films. With this preparation, the surface-to-volume ratio and the porous feature are enhanced; thus, the nanoparticulate films are suitable for physical and chemical reactions on the surface. The nanoparticulate $(WO_3)_{87.5}(MoO_3)_{12.5}$ composite film based on sample WMo-20 is given as a negative electrode, and another empty fluorine tin oxide (FTO) glass substrate is used as a positive electrode for the assembly of a supercapacitive ESD. To demonstrate the function of the ESDs, two ESDs are connected in series to double the driving voltage for lighting up a light-emitting diode (LED). Figure 1C illustrates the initial state and the charged (colored) state of the supercapacitive ESDs. The two series-connected ESDs are charged for ~3 min, with −8 V applied on one negative electrode and one positive electrode grounded. The charged ESDs are then connected to an LED. Figure 1D exposes the lighting up of an LED and the variation of the potential as a function of time across the two ESDs. The period of the LED lighting up is longer than 8.5 min, with a stable change of discharging voltages from −2.45 to −2.30 V. The period is longer than that of the ~2 min measured in our previous studies.[5] The energy storage capability of the ESDs is promoted simply due to the increment of the nanoparticulate film thickness. The energy storage capability is further investigated with regard to the thickness of the nanoparticulate $(WO_3)_{87.5}(MoO_3)_{12.5}$ composite films.

Cyclic voltammetry (CV) of WO_3/MoO_3 composite films

Energy storage capabilities of the nanoparticulate $(WO_3)_{87.5}(MoO_3)_{12.5}$ composite films are inspected by either CV or galvanostatic charge-discharge (GCD) curves. Figure 2A exhibits the CV curves of samples WMo-05 to WMo-20 at a scan rate of 20 mV/s, with a scan direction indicated. For samples WMo-16 and WMo-20, a wider potential window from −2.0 to 2.0 V is used because the redox peaks shift to higher voltages. All CV curves reveal reversible redox reactions in loops, implying an insertion and extraction of Li^+ ions. Meanwhile, the color of the nanoparticulate film changes to dark blue from the original transparent at negative voltages when Li^+ ions are intercalated into $(WO_3)_{87.5}(MoO_3)_{12.5}$ composites. In the deintercalated process at positive voltages, the films return to their transparent (bleached) color. The CV loops are enlarged with an increase in film thickness that infers many more Li^+ ions stored in the supercapacitive materials.

In the oxidation and reduction processes, the highest currents in the loop give anodic (deintercalation) and cathodic (intercalation) peak currents for the evaluation of diffusion coefficients (D) of Li^+ ions in the nanoparticulate films. The diffusion coefficient at 25°C is evaluated through the Randles-Sevcik equation: $j_p = 2.69 \times 10^5 n^{3/2} D^{1/2} C v^{1/2}$, where $n = 1$ is the number of electrons transferred in the redox

Please cite this article in press as: Wei et al., Boosting areal capacitance in WO_3-based supercapacitor materials by stacking nanoporous composite films, Cell Reports Physical Science (2024), https://doi.org/10.1016/j.xcrp.2024.101836

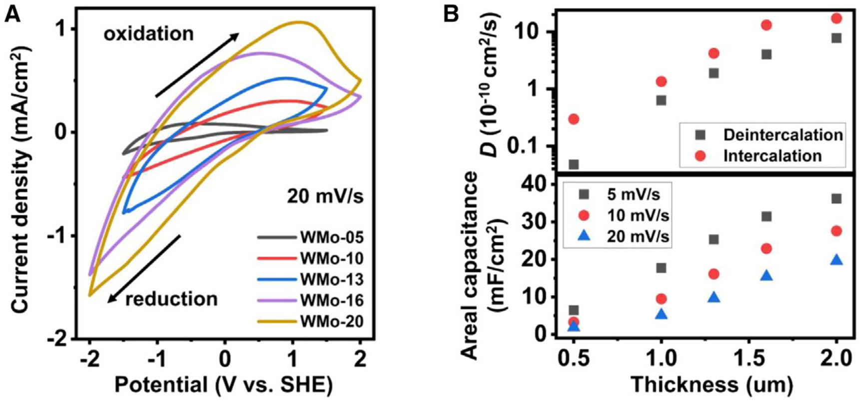

Figure 2. CV measurement

(A) CVs of samples WMo-05, WMo-10, WMo-13, WMo-16, and WMo-20 at a voltage scanning rate of 20 mV/s. The voltage scanning direction is indicated on the graph.

(B) Diffusion coefficients and areal capacitances of nanoparticulate $(WO_3)_{87.5}(MoO_3)_{12.5}$ films as a function of film thickness. The red circles and the black squares at top represent diffusion coefficients obtained in reduction (intercalation) and oxidation (deintercalation) processes, respectively. The black squares, the red circles, and the blue triangles at bottom give the areal capacitance evaluated at voltage scanning rates of 5, 10, and 20 mV/s, respectively.

reaction, C is the concentration of electrolyte, and v is the scan rate of the sweeping potential.

The diffusion coefficients for intercalation and deintercalation are 2.96×10^{-11} and 5.51×10^{-10} cm^2/s for sample WMo-05 that are much smaller than the values of 3.39×10^{-10} and 1.18×10^{-10} cm^2/s obtained previously,[5] owing mainly to the decrement of the scan rate from 150 to 20 mV/s. In the present study, the diffusion coefficients for intercalation and deintercalation significantly increase up to 1.72×10^{-9} and 7.78×10^{-10} cm^2/s for sample WMo-20 at the slow scan rate of 20 mV/s. The diffusion coefficients in the logarithmic scale as a function of the nanoparticulate $(WO_3)_{87.5}(MoO_3)_{12.5}$ film thickness are exposed in the upper panel of Figure 2B. The diffusion coefficient increases exponentially with an increase in the nanoparticulate film thickness. The nature of Li^+ ion diffusion in the electrolyte does not change, whereas the $(WO_3)_{87.5}(MoO_3)_{12.5}$ films for the embodiment of ion diffusion and redox reactions are extended from two-dimensional (thin film) to three-dimensional (thick film) structures. Such an extension leads to the outcome of exponentially raised diffusion coefficients. As revealed in Figure 2B, the diffusion coefficient of intercalation is ~2–3 times higher than that of deintercalation for thicker films, whereas it is ~6 times higher for sample WMo-05. For the thicker nanoporous film, the surface area expands exponentially, which accelerates ion intercalation and deintercalation near the surface without diffusing deeply into the crystalline bulk. Thus, the difference in diffusion coefficients between the intercalation and deintercalation processes becomes smaller. In addition, we adopt another method to estimate the diffusion coefficient. Figures S9A–S9D exhibit the CV curves of samples WMo-05, WMo-13, WMo-20, and WMo-180 at scan rates (v) from 2 to 20 mV/s. The linear least-squares fitting to the data of the peak current density (j_p) and $v^{1/2}$ give slopes that are used to estimate diffusion coefficients at 25°C.[34–36] Figure S9E shows the j_p as a function of the square root of the voltage scan rate. The inset to Figure S9F points to the same feature of an exponential increase in the diffusion coefficient as a function of the film thickness. For the film that is ~18 μm in thickness in Figure S9F, the diffusion coefficient seems not to increase so rapidly, which is in line with methanol diffusion in poly(vinyl acetate)

Please cite this article in press as: Wei et al., Boosting areal capacitance in WO_3-based supercapacitor materials by stacking nanoporous composite films, Cell Reports Physical Science (2024), https://doi.org/10.1016/j.xcrp.2024.101836

films.[37] In addition, the diffusion coefficients of intercalation and deintercalation for the thickest film reach up to 1.12×10^{-7} and 3.19×10^{-8} cm^2/s, which are almost the highest values ever recorded.

The CV curves are also used for the evaluation of areal capacitances according to the equation $C_{areal} = (\int Jdt)/(2v \cdot \Delta V)$, where J is the current density, v is the scan rate, and ΔV is the voltage range of the potential window. The C_{areal} as a function of nanoparticulate film thickness is offered in the lower panel of Figure 2B. The C_{areal} at the scan rate of 5 mV/s is ~6.46 mF/cm^2 for sample WMo-05 and it is increased ~5.6 times up to 36.2 mF/cm^2 for sample WMo-20. The C_{areal}'s for sample WMo-20 are 36.2, 27.6, and 19.6 mF/cm^2 at scan rates of 5, 10, and 20 mV/s. The C_{areal} decreases with an increasing scan rate for thicker films, whereas it does not change considerably for thin films such as in sample WMo-05. The higher C_{areal} at a lower scan rate implies sufficient time for Li^+ ion diffusion in nanoparticulate $(WO_3)_{87.5}(MoO_3)_{12.5}$ films.

To analyze the charge storage mechanism, the data of current densities and voltage scan rates are fitted according to the equation $j_p = a\nu^b$,[38–40] where a is a constant, ν is the voltage scan rate, j_p is the redox peak current density, and b is the exponent. The exponent b shall theoretically be in the range of 0.5–1. Figure S10 presents the data of $\log(j_p)$ as a function of $\log(v)$ for samples WMo-05, WMo-13, WMo-20, and WMo-180, and the b values are the slopes of those linear fittings. The exponent b in ion intercalation does not vary with increasing thickness, whereas the b in ion deintercalation decreases from 0.97 to 0.51. It implies a transition of the mechanism from the EDLC to the pseudocapacitor during the discharging process. Electrochemical impedance spectroscopies of samples WMo-05, WMo-20, and WMo-180 are provided in Figure S11. The data do not show noticeable semicircles in the high-frequency region that indicate a capacitive behavior. Moreover, the straight-line feature in the low-frequency region suggests a low ion diffusion resistance, making them promising for supercapacitor applications. The intercept on the real impedance axis (Z′) represents the equivalent series resistance (R_s) of 87.9, 86.1, and 88.1 $\Omega \cdot cm^2$ for samples WMo-05, WMo-20, and WMo-180, respectively.

GCD of WO_3/MoO_3 composite films

The measurement of GCD curves provides another method to assess the energy storage capability of the nanoparticulate films. It is measured at a constant current supplied to the nanoparticulate film for both charging and discharging processes, and the voltage is recorded as a function of time. In this study, GCD curves at several different current densities are collected for the estimation of the specific capacitance. Figure 3A unveils GCD curves of samples WMo-05–WMo-20 at a current density of 0.1 mA/cm^2 and a GCD curve of sample WMo-180 at a current density of 0.5 mA/cm^2. For the thickest film of sample WMo-180, the GCD cycle takes a much longer time at a low current density; thus, a higher current density of 0.5 mA/cm^2 is used. When the thickness of the nanoparticulate $(WO_3)_{87.5}(MoO_3)_{12.5}$ film increases, the charging and discharging time increases. For all of the samples, the charging time is very close to the discharging time, which implies a relatively high reversibility in electrochemical reactions.[41] The discharging curve of sample WMo-180 deviates away from the ideal triangular shape that indicates the redox process and manifests itself as pseudocapacitor- and battery-type materials. The areal capacitance is extracted using the equation $C_{areal} = (J\Delta t)/\Delta V$, where J is the discharging current density, Δt is the discharging time, and ΔV is the voltage range of the potential window. From the GCD curves, the C_{areal}'s are estimated to be 15.45 and 87.27 mF/cm^2 for samples WMo-05 and WMo-20. Those areal capacitances are ~2.4 times higher than the values of 6.46 and 36.2 mF/cm^2 obtained

Please cite this article in press as: Wei et al., Boosting areal capacitance in WO_3-based supercapacitor materials by stacking nanoporous composite films, Cell Reports Physical Science (2024), https://doi.org/10.1016/j.xcrp.2024.101836

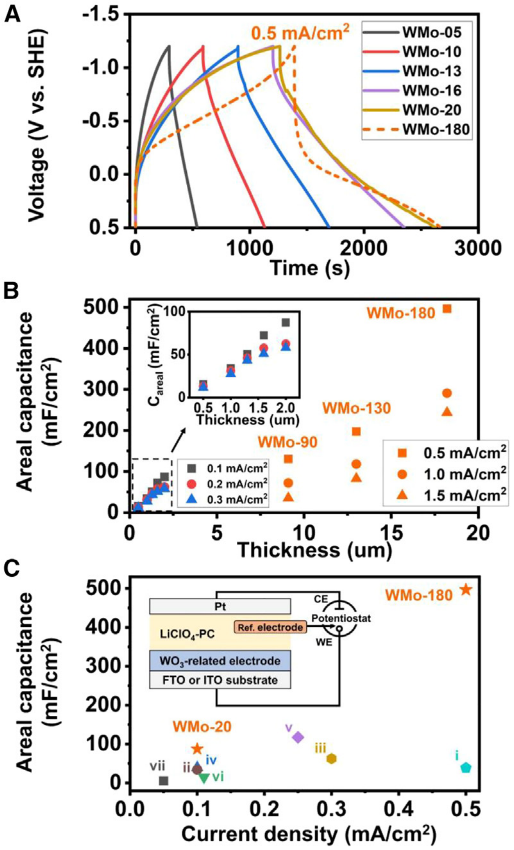

Figure 3. GCD measurement and comparison of areal capacitance

(A) GCD curves of samples WMo-05, WMo-10, WMo-13, WMo-16, and WMo-20 at a constant current density of 0.1 mA/cm^2 and of sample WMo-180 at 0.5 mA/cm^2.

(B) Areal capacitances of nanoparticulate $(WO_3)_{87.5}(MoO_3)_{12.5}$ films as a function of film thickness at current densities of 0.1 (black squares), 0.2 (red circles), and 0.3 mA/cm^2 (blue triangles). The orange symbols point to the areal capacitances of the film, with thicknesses of ~9.0, 13, and 18 μm, measured at current densities of 0.5, 1.0, and 1.5 mA/cm^2. The inset shows a magnified area of the dashed-line rectangle.

(C) Areal capacitances at various current densities of our samples and other groups' materials, including (i) WO_3-V_2O_5 composites,[22] (ii) porous P5Fin/WO_3 nanocomposites,[23] (iii) Gd-doped WO_3 nanofilms,[45] (iv) Mo-doped α-WO_3 thin films,[46] (v) Mo-doped WO_3 thin films,[47] (vi) WO_3-ZnO composite thin films,[44] and (vii) WO_3/PEDOT:PSS films.[48] The inset gives the configuration of the areal capacitance measurements.

from the CV curves at the scan rate of 5 mV/s. In particular, the areal capacitance of sample WMo-180 gives an outstanding benchmarked value of 496 mF/cm^2

Figure 3B shows the areal capacitance as a function of the thickness of the nanoparticulate $(WO_3)_{87.5}(MoO_3)_{12.5}$ film. High current densities are used in GCD measurements for samples WMo-90, WMo-130, and WMo-180. The areal capacitances are estimated at the 10th loop of the GCD curve. With current densities increased from 0.1 to 0.3 mA/cm^2, the areal capacitance of the thinnest film (sample WMo-05) does not vary apparently, whereas that of sample WMo-20 shows a significant variation, giving a lower areal capacitance at a higher current density. For sample WMo-20, the C_{areal} of 87.3 mF/cm^2 at 0.1 mA/cm^2 drops down to 62.4 and 58.2 mF/cm^2 at current densities of 0.2 and 0.3 mA/cm^2, respectively. The same trend is observed for thicker films of samples WMo-90, WMo-130, and WMo-180 that the areal capacitance of the thickest film (WMo-180) reveals an abrupt decrease, with current densities increased from 0.5 to 1.5 mA/cm^2. Alternatively, the areal capacitance does increase monotonically with the increasing film thickness, which indicates the capability of the stacking features for nanoparticulate materials. It is worth noting that the C_{areals} of sample WMo-180 are 496, 291, and 243 mF/cm^2 at 0.5, 1.0, and 1.5 mA/cm^2, respectively. The effective diffusion length of Li^+ ions in thick films is longer, but the diffusion requires a longer time under the high current density. A longer diffusion time is required for a thick nanoporous film with a high areal current; thus, the C_{areal} descends with increasing current densities.[42,43] Here, the C_{areal} decreases with an increase in the current density, and the rate capability is used for such an evaluation. For example, the rate capabilities of samples WMo-05 and WMo-20 are ~75.4% and ~66.7%, respectively, with a current density increased from 0.1 to 0.3 mA/cm^2. For sample WMo-180, it significantly decreases to ~48.9%, with current densities tripled from 0.5 to 1.5 mA/cm^2. Similar trends have been reported previously. For example, the rate capability is ~61.9% for P5FIn/WO_3 nanocomposites[23] when the current density increases from 0.03 to 0.1 mA/cm^2. It is ~77% for WO_3-ZnO composites,[44] with current densities varying from 0.3 to 1.1 mA/cm^2, and it is ~77% for WO_3/graphene/polyaniline films, with current densities changed from 0.05 to 0.15 mA/cm^2

The outstanding C_{areal} of 87.3 and 496 mF/cm^2 for sample WMo-20 and WMo-180 are benchmarked against recent works such as 38.75 mF/cm^2 for WO_3-V_2O_5 composites,[22] 34.1 mF/cm^2 for porous P5FIn/WO_3 nanocomposites,[23] 62.43 mF/cm^2 for Gd-doped WO_3 nanofilms,[45] 39.2 mF/cm^2 for Mo-doped α-WO_3 thin films,[46] 117.1 mF/cm^2 for Mo-doped WO_3 thin films,[47] 15.24 mF/cm^2 for WO_3-ZnO composite thin films,[44] and 5.3 mF/cm^2 for WO_3/poly(3,4-ethylenedioxythiophene) polystyrene sulfonate (PEDOT:PSS) films.[48] The comparison is summarized in Figure 3C, with the current density indicated. It is noted that sample WMo-20 exhibits a comparably high C_{areal}, whereas the film thickness can be piled up to further aggrandize and raise the C_{areal}. Sample WMo-180 shows the highest C_{areal}, which is more than five times higher than those reported previously, and it is measured in the same three-electrode system, consisting of a Pt counterelectrode, an $LiClO_4$ electrolyte, and an FTO (or InSn) current collector.

Gravimetric capacitance of WO_3/MoO_3 composite films

The gravimetric capacitance in F/g units is calculated to explore more about the energy storage mechanism in the nanoporous films. We calculate the loading mass for all of our samples as described in detail in the supplemental experimental procedures. For example, the mass loadings for samples WMo-20 and WMo-180 are evaluated to be ~0.95 and 9.5 mg/cm^2. The gravimetric capacitance of samples WMo-20 and WMo-180 at 0.1 and 0.05 A/g are calculated to be ~91.9 and 52.2 F/g, respectively, which are higher than the 24 F/g for WO_3 coated on glassy carbon substrates[49] and lower than 436 F/g at 1 A/g for WO_3 nanofibers.[19] Figure 4A displays gravimetric capacitances of nanoparticulate $(WO_3)_{87.5}(MoO_3)_{12.5}$ composite films with a thickness of less than 2.0 μm at lower current densities of 0.1, 0.2, and 0.3 mA/cm^2. At the current density of 0.1 mA/cm^2, gravimetric capacitances of all of the samples vary between ~81.3 and ~91.9 F/g. In addition, the gravimetric capacitance increases to a maximum and decreases with increasing film thickness. The decrease in gravimetric capacitance comes from the stacking nature of the increment of the third dimension of the film thickness. Similar behaviors have been reported in the literature.[50] Li et al. report that the gravimetric capacitance decreases when the thickness of their films increases. The feature could be attributed to a gradual loss of surface conductivity in thicker films.[50] Figure 4B presents gravimetric capacitances

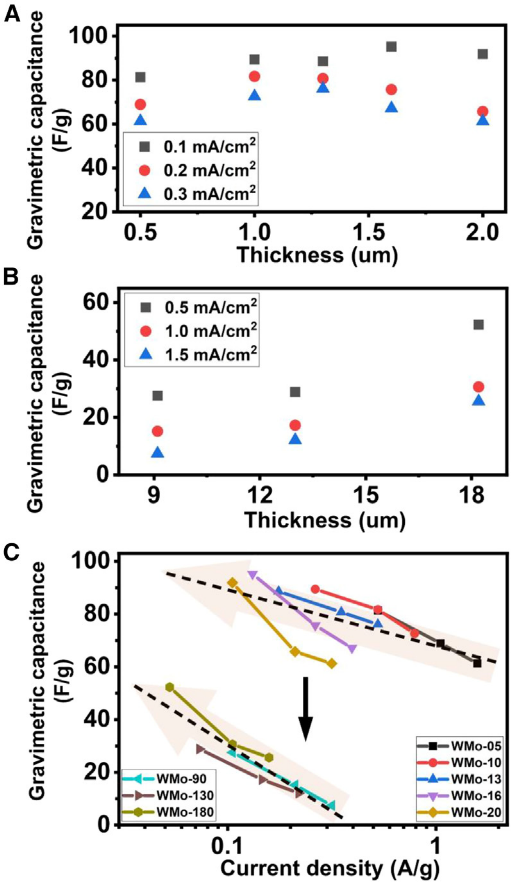

Figure 4. Comparison of gravimetric capacitance

(A) Gravimetric capacitance of $(WO_3)_{87.5}(MoO_3)_{12.5}$ composite films with a thickness of less than 2.0 μm at discharging current densities of 0.1, 0.2, and 0.3 mA/cm^2.

(B) Gravimetric capacitance of $(WO_3)_{87.5}(MoO_3)_{12.5}$ composite films with a thickness greater than 9.0 μm under discharging current densities of 0.5, 1.0, and 1.5 mA/cm^2. (C) Gravimetric capacitance of all of the samples as a function of gravimetric current density in logarithmic scale. The black dashed lines are the least-squares fitting lines to data in the low- and high-current density groups.

for thicker composite films at a current density higher than 0.5 mA/cm^2. The gravimetric capacitance increases with an increase in film thickness that indicates the potential to raise the gravimetric capacitance further with NP stacking. However, the gravimetric capacitance significantly decreases to ~52.2 F/g due to a high areal current density, indicating that the ions in the electrolyte must take a longer time to diffuse in the third dimension (the thickness) of the nanoporous composite films.

The gravimetric capacitances of all of the samples with respect to gravimetric current density are shown in Figure 4C. The data are categorized into two groups, with one measured at areal current densities smaller than 0.5 mA/cm^2 and the other measured at a higher areal current density. In the group of low areal current densities, the highest gravimetric capacitance of 95.2 F/g is obtained at 0.13 A/g for sample WMo-16. However, the gravimetric capacitance presents an incremental tendency with increasing film thickness at a decreasing gravimetric current density. The results highlight the tradeoff between the areal and the gravimetric capacitances when the nanoporous composite film expands in the direction of the film thickness. It was argued in the reference papers of Wang et al.[54] that the weight of the substrate as well as the

Please cite this article in press as: Wei et al., Boosting areal capacitance in WO_3-based supercapacitor materials by stacking nanoporous composite films, Cell Reports Physical Science (2024), https://doi.org/10.1016/j.xcrp.2024.101836

electrode should be included in the estimation of gravimetric power density and energy density. That may underscore the importance of the scalable technique over pursuing a high gravimetric capacitance.[51] Furthermore, the measurement of the mass of working materials usually produces significant errors that lead to overstatements of performance.[52] As a consequence, the areal and gravimetric capacitances are essential in the applications of different directions, and, in some situations, the concept of areal capacitance plays a larger role in performance characterization.[53]

The energy storage capability of the $(WO_3)_{87.5}(MoO_3)_{12.5}$ composite films shall depend largely on the electrolyte used in the GCD measurements. To investigate its variation, we also performed GCD measurements for sample WMo-20 under the electrolyte of 1 M H_2SO_4. Figure S12A presents the GCD curves at a high constant current density of 1.0 mA/cm^2 within the potential window between −0.4 and 0.5 V. The GCD curves have a moderately symmetric feature between the charging and discharging processes that points to a high electrochemical reversibility. The $C_{areal}'s$ of the 1st and 10th cycles are estimated to be 151.7 and 121.9 mF/cm^2. Comparing this with that in the electrolyte of 1 M $LiClO_4$ + propylene carbonate (PC), the applied current density is 10 times higher and the potential window is approximately one-half smaller in the GCD measurements in 1 M H_2SO_4. Figure S12B provides a comprehensive comparison of the C_{areal} of the nanoparticulate $(WO_3)_{87.5}(MoO_3)_{12.5}$ composite films, obtained in electrolytes of 1 M H_2SO_4 and 1 M $LiClO_4$ + PC at different current densities. It is noted that for the electrolyte of 1 M $LiClO_4$ + PC, the C_{areal} is expected to be lower than 87.3 mF/cm^2. Nevertheless, it increases to 114.1 mF/cm^2 when the electrolyte of 1 M H_2SO_4 is applied to the GCD measurements. These results signify the important roles of electrolytes for the estimation of the specific capacitance.

Retention ability and performance of symmetric devices

The retention ability of the energy storage capability is further explored through the GCD measurements on samples WMo-20 and WMo-90 at current densities of 1.8 and 2.8 mA/cm^2, respectively. Figures 5A and 5C exhibit several cycles of charging and discharging GCD curves for samples WMo-20 and WMo-90 within a potential window in the range between 1.2 and −0.8 V. For sample WMo-20, the charging and discharging time continuously decreases, as indicated by the orange arrow, whereas the charging and discharging time of sample WMo-90 increases in the first 160 cycles and starts to decrease thereafter until the end.

According to the GCD curves, the retention of areal capacitance and the Coulombic efficiency of samples WMo-20 and WMo-90 for 5,000 cycles are evaluated and given in Figures 5B and 5D. The insets to Figures 5B and 5D offer the corresponding areal capacitance with respect to cycle number. The capacitance retention of sample WMo-20 exhibits a stable decay to 60% of its initial value. The areal capacitance at 1.8 mA/cm^2 in the 1st and the 5,000th cycles are 27.8 and 15.9 mF/cm^2, respectively. For sample WMo-90, the areal capacitance at 2.8 mA/cm^2 is ∼59.3 mF/cm^2 in the beginning and it decreases to 46.6 mF/cm^2 in the 5,000th cycle. The capacitance retention of sample WMo-90 surpasses 100% within ∼1,000 cycles (see the red dashed line frame in Figure 5D), and it reaches the highest value of ∼139% in the 160th cycle. This phenomenon is in line with that reported in the literature.[54] It could be attributed to more and more mixed regions of partially active and inactive regions in thicker films. These regions are activated after certain cycles of charging and discharging GCD measurements, and the retention ability could surpass its initial state, especially for thicker nanoporous films. The Coulombic efficiency of both samples changes a little bit and remains at ∼99.6% and 99.7% of their original value throughout the measurement.

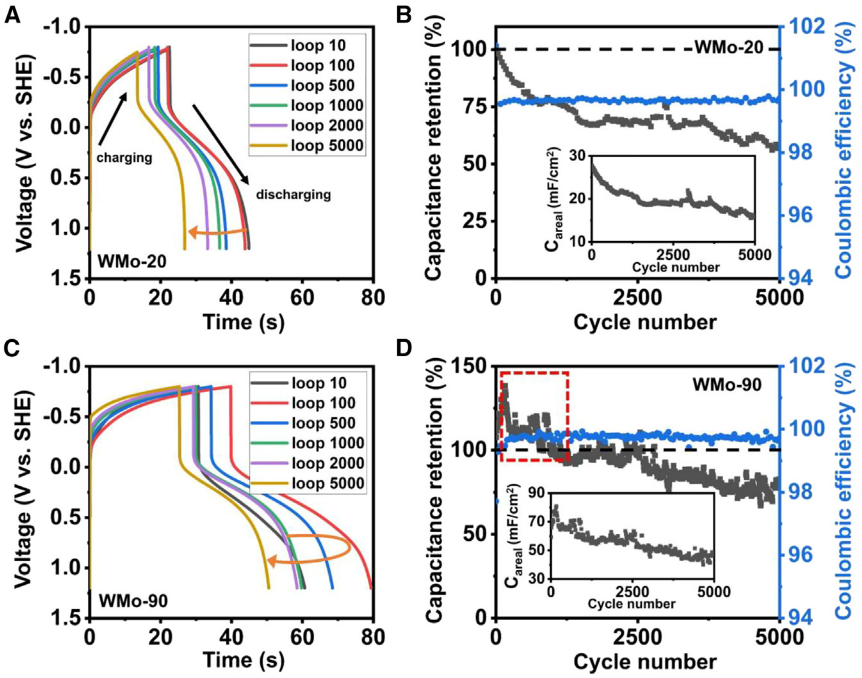

Figure 5. Capacitance retention test

(A) Several loops of GCD curves of sample WMo-20 in the voltage range from 1.2 to −0.8 V at a current density of 1.8 mA/cm^2. The orange arrow provides a guide to the variation according to the GCD loop number.

(B) Retention rate of capacitance (black squares) and Coulombic efficiency (blue dots) of sample WMo-20 as a function of cycle number, measured at a current density of 1.8 mA/cm^2.

(C) Several loops of GCD curves of sample WMo-90 at voltages ranging from 1.2 to −0.8 V at a current density of 2.8 mA/cm^2. The orange arrow shows the evolution trend of the GCD curve with an increment of cycle number.

(D) Capacitance retention (black squares) and Coulombic efficiency (blue dots) of sample WMo-90 as a function of cycle number, measured at a current density of 2.8 mA/cm^2. The red dashed-line frame points to the region where the capacitance retention surpasses 100%. The insets to Figures 5B and 5D offer areal capacitances as a function of cycle number.

The results imply a good retention ability of energy storage for nanoparticulate $(WO_3)_{87.5}(MoO_3)_{12.5}$ composite films. The GCD curves and areal capacitances above are measured in a three-electrode potentiostat. To check the areal capacitances of ECDs, we prepared a symmetric supercapacitive ESD (see Figure S13A) based on sample WMo-20. The GCD measurements at a current density of 0.1 mA/cm^2 are depicted in Figure S13B. The GCD measurements are carried out in the potential window ranging from −1.5 to 1.5 V. The areal capacitance of the symmetric supercapacitive ECD is ~18.1 mF/cm^2, which is approximately one-fifth of the areal capacitance of the film measured in the potentiostat.

Overall, the nanoporous $(WO_3)_{1-x}(MoO_3)_x$ composite film presents promise for scalability toward both areal and gravimetric supercapacitive applications. This study is one entry in the increasing efforts to design and implement high-capacity EC and ESDs.

EXPERIMENTAL PROCEDURES

Resource availability

Lead contact

Further information and requests for resources and reagents should be directed to and will be fulfilled by the corresponding author, Wen-Bin Jian (wbjian@nycu.edu.tw).

Please cite this article in press as: Wei et al., Boosting areal capacitance in WO_3-based supercapacitor materials by stacking nanoporous composite films, Cell Reports Physical Science (2024), https://doi.org/10.1016/j.xcrp.2024.101836

Materials availability

This study did not generate new unique materials.

Data and code availability

All of the datasets used in this study are available within the article and are described in the supplemental information or are available from the corresponding author upon reasonable request. There was no code generated in this study.

MoO_3 and WO_3 NPs suspension production

MoO_3 and WO_3 NPs were synthesized in deionized water by the electroexploding wire technique at a direct current voltage of 36 V using an NP generator (Metal Xano, Nanovie, Taiwan). The concentration of either MoO_3 or WO_3 NP suspension was estimated to be $\sim 4 \times 10^{-3}$ M and it was simply mixed to prepare $(WO_3)_{87.5}(MoO_3)_{12.5}$ suspensions.

$(WO_3)_{1\text{-}x}(MoO_3)_x$ composite film deposition

The mixed NP suspensions were used to deposit nanoporous, nanoparticulate films on the FTO glass by a spray coater (Xano Spray Coating, Nanovie). The FTO glasses, having a thickness of 2.2 mm and a sheet resistance of 7 Ω/sq, were purchased from Rui Long Optoelectronics (Taiwan). During the spray-coating deposition, the FTO glass substrates were heated at 300°C on a hot plate and the spray nozzle was kept at a distance of 9 cm away from the substrate. The details about preparations and characterizations of NPs and $(WO_3)_{1\text{-}x}(MoO_3)_x$ composite films were described in our previous paper.[5]

WO_3/MoO_3 supercapacitor ESD

The fabrication of supercapacitive ESDs with $(WO_3)_{87.5}(MoO_3)_{12.5}$ composite films on the negative electrode was described as follows. $(WO_3)_{87.5}(MoO_3)_{12.5}$ suspensions were spray coated on an FTO glass substrate with an area of 4.0×3.5 cm^2 that was used as a negative electrode for the supercapacitive ESDs. The coated FTO glass substrate was affixed on its four edges with frame spacers using double-sided acrylic tape (Kinsten Industrial, Taiwan) with a thickness of 1 mm. Another empty FTO glass substrate was attached on the acrylic tape on the positive electrode to form a supercapacitive ESD. The edges of the ESD were sealed with a UV sealant (Padico, Japan) while leaving a small hole for the injection of the electrolyte. Finally, a 1-M $LiClO_4$ + PC electrolyte[5] was injected into the ESD using a syringe mounted with a sharp needle. The working area of the ESD was $\sim 4.0 \times 3.5$ cm^2. The same procedure was applied to fabricate symmetric ESDs in which $(WO_3)_{87.5}(MoO_3)_{12.5}$ composite films were coated on the two opposite FTO glass substrates of the symmetric ESD.

Characterization

Morphologies and lattice structures of WO_3 and MoO_3 NPs were inspected using TEM (JEOL ARM200F, Japan). The thicknesses of the nanoparticulate $(WO_3)_{87.5}(MoO_3)_{12.5}$ films on the FTO glass substrates were measured using an SEM (Hitachi SU-8010, Japan), and the surfaces of the films were inspected using an AFM (SPA300HV, Seiko Instruments, Japan). The Raman spectra of the nanoparticulate films on the FTO substrates were taken with a 532-nm laser source by a Raman spectroscope (MRI, ProTrustTech, Taiwan). Crystalline structures were examined using XRD (D8 Advance, Bruker AXS, Germany) with a Cu Kα radiation source (λ = 1.5406 Å). Surface electronic states of nanoparticulate films were collected using XPS (PHI 5000 VersaProbe, UlVAC-PHI Instruments, Japan). CV and GCD measurements were performed in a three-electrode system using a potentiostat (SP-50 Potentiostat, BioLogic, France). Electrochemical impedance spectroscopy data were collected using an electrochemical station (Autolab PGSTAT302N, Metrohm AG, Switzerland). Pt meshes were used for the counterelectrode, and the reference electrode was the standard hydrogen electrode. The 1 M $LiClO_4$ + PC electrolyte was used in the potentiostat. The voltage scanning rates of 2, 5, 10, and 20 mV/s were adopted in the CV measurements, and the current densities of 0.1, 0.2, 0.3, 0.5, 1.0, and 1.5 mA/cm^2 were applied in the GCD measurements.

SUPPLEMENTAL INFORMATION

Supplemental information can be found online at https://doi.org/10.1016/j.xcrp.2024.101836.

ACKNOWLEDGMENTS

This work was supported by the National Science and Technology Council, Taiwan, under grant nos. NSTC-111-2124-*M*-A49-008 and NSTC-111-2112-*M*-A49-038. This work was also financially supported by the Center for the Semiconductor Technology Research from the Featured Areas Research Center Program within the framework of the Higher Education Sprout Project by the Ministry of Education, Taiwan, and supported in part by the National Science and Technology Council, Taiwan, under grant no. NSTC 111-2634-F-A49-008.

AUTHOR CONTRIBUTIONS

Conceptualization, C.-C.W. and W.-B.J. Methodology, C.-C.W. and W.-B.J. Investigation, C.-C.W., P.-H.L., C.-E.H., Y.-L.L., S.B., and A.P.K. Formal analysis, C.-C.W. Validation, W.-B.J. Writing – original draft, C.-C.W. Writing – review & editing, W.-B.J. Resources, J.-T.C., C.-W.C., R.-A.D., and K.T. Project administration, W.-B.J. Supervision, K.T. Funding acquisition, W.-B.J. The manuscript was written through the contributions of all of the authors. All of the authors have given approval to the final version of the manuscript.

DECLARATION OF INTERESTS

The authors declare no competing interests.

Received: October 20, 2023
Revised: December 21, 2023
Accepted: January 25, 2024
Published: February 26, 2024

REFERENCES

1. González-Torres, M., Pérez-Lombard, L., Coronel, J.F., Maestre, I.R., and Yan, D. (2022). A review on buildings energy information: Trends, end-uses, fuels and drivers. Energy Rep. *8*, 626–637. https://doi.org/10.1016/j.egyr.2021.11.280.
2. Simon, P., and Gogotsi, Y. (2008). Materials for electrochemical capacitors. Nat. Mater. *7*, 845–854. https://doi.org/10.1038/nmat2297.
3. Khaligh, A., and Li, Z. (2010). Battery, Ultracapacitor, Fuel Cell, and Hybrid Energy Storage Systems for Electric, Hybrid Electric, Fuel Cell, and Plug-In Hybrid Electric Vehicles: State of the Art. IEEE Trans. Veh. Technol. *59*, 2806–2814. https://doi.org/10.1109/TVT.2010.2047877.
4. Wu, W., Wang, M., Ma, J., Cao, Y., and Deng, Y. (2018). Electrochromic Metal Oxides: Recent Progress and Prospect. Adv. Electron. Mater. *4*, 1800185. https://doi.org/10.1002/aelm.201800185.
5. Wei, C.-C., Wu, T.-H., Huang, J.-W., Young, B.-L., Jian, W.-B., Lin, Y.-L., Chen, J.-T., Hsu, C.-S., Ma, Y.-R., and Tsukagoshi, K. (2023). Nanoparticulate films of WO_3 and MoO_3 composites for enhancing UV light electrochromic transmittance variation and energy storage applications. Electrochim. Acta *442*, 141897. https://doi.org/10.1016/j.electacta.2023.141897.
6. Chang, C.-M., Chiang, Y.-C., Cheng, M.-H., Lin, S.-H., Jian, W.-B., Chen, J.-T., Cheng, Y.-J., Ma, Y.-R., and Tsukagoshi, K. (2021). Fabrication of WO_3 electrochromic devices using electro-exploding wire techniques and spray coating. Sol. Energy Mater. Sol. Cells *223*, 110960. https://doi.org/10.1016/j.solmat.2021.110960.
7. Yang, P., Sun, P., and Mai, W. (2016). Electrochromic energy storage devices. Mater. Today *19*, 394–402. https://doi.org/10.1016/j.mattod.2015.11.007.
8. May, G.J., Davidson, A., and Monahov, B. (2018). Lead batteries for utility energy storage: A review. J. Energy Storage *15*, 145–157. https://doi.org/10.1016/j.est.2017.11.008.
9. Kim, T., Song, W., Son, D.-Y., Ono, L.K., and Qi, Y. (2019). Lithium-ion batteries: outlook on present, future, and hybridized technologies. J. Mater. Chem. A *7*, 2942–2964. https://doi.org/10.1039/C8TA10513H.
10. Pandolfo, A.G., and Hollenkamp, A.F. (2006). Carbon properties and their role in supercapacitors. J. Power Sources *157*, 11–27. https://doi.org/10.1016/j.jpowsour.2006.02.065.

11. Ruiz, V., Roldán, S., Villar, I., Blanco, C., and Santamaría, R. (2013). Voltage dependence of carbon-based supercapacitors for pseudocapacitance quantification. Electrochim. Acta *95*, 225–229. https://doi.org/10.1016/j.electacta.2013.02.056.
12. Milekhin, A.G., Yeryukov, N.A., Sveshnikova, L.L., Duda, T.A., Kosolobov, S.S., Latyshev, A.V., Surovtsev, N.V., Adichtchev, S.V., Himcinschi, C., Zenkevich, E.I., et al. (2012). Raman Scattering for Probing Semiconductor Nanocrystal Arrays with a Low Areal Density. J. Phys. Chem. C *116*, 17164–17168. https://doi.org/10.1021/jp210720v.
13. Ou, Y.C., Cheng, S.F., and Jian, W.B. (2009). Size dependence in tunneling spectra of PbSe quantum-dot arrays. Nanotechnology *20*, 285401. https://doi.org/10.1088/0957-4484/20/28/285401.
14. Choudhary, N., Li, C., Moore, J., Nagaiah, N., Zhai, L., Jung, Y., and Thomas, J. (2017). Asymmetric Supercapacitor Electrodes and Devices. Adv. Mater. *29*, 1605336. https://doi.org/10.1002/adma.201605336.
15. Kim, H., and Popov, B.N. (2002). Characterization of hydrous ruthenium oxide/carbon nanocomposite supercapacitors prepared by a colloidal method. J. Power Sources *104*, 52–61. https://doi.org/10.1016/S0378-7753(01)00903-X.
16. Brousse, T., Taberna, P.-L., Crosnier, O., Dugas, R., Guillemet, P., Scudeller, Y., Zhou, Y., Favier, F., Bélanger, D., and Simon, P. (2007). Long-term cycling behavior of asymmetric activated carbon/MnO_2 aqueous electrochemical supercapacitor. J. Power Sources *173*, 633–641. https://doi.org/10.1016/j.jpowsour.2007.04.074.
17. Li, H., McRae, L., Firby, C.J., Al-Hussein, M., and Elezzabi, A.Y. (2018). Nanohybridization of molybdenum oxide with tungsten molybdenum oxide nanowires for solution-processed fully reversible switching of energy storing smart windows. Nano Energy *47*, 130–139. https://doi.org/10.1016/j.nanoen.2018.02.043.
18. Upadhyay, K.K., Altomare, M., Eugénio, S., Schmuki, P., Silva, T.M., and Montemor, M.F. (2017). On the Supercapacitive Behaviour of Anodic Porous WO_3-Based Negative Electrodes. Electrochim. Acta *232*, 192–201. https://doi.org/10.1016/j.electacta.2017.02.131.
19. Zheng, F., Xi, C., Xu, J., Yu, Y., Yang, W., Hu, P., Li, Y., Zhen, Q., Bashir, S., and Liu, J.L. (2019). Facile preparation of WO_3 nano-fibers with super large aspect ratio for high performance supercapacitor. J. Alloys Compd. *772*, 933–942. https://doi.org/10.1016/j.jallcom.2018.09.085.
20. Lokhande, V., Lokhande, A., Namkoong, G., Kim, J.H., and Ji, T. (2019). Charge storage in WO_3 polymorphs and their application as supercapacitor electrode material. Results Phys. *12*, 2012–2020. https://doi.org/10.1016/j.rinp.2019.02.012.
21. Sun, K., Hua, F., Cui, S., Zhu, Y., Peng, H., and Ma, G. (2021). An asymmetric supercapacitor based on controllable WO_3 nanorod bundle and alfalfa-derived porous carbon. RSC Adv. *11*, 37631–37642. https://doi.org/10.1039/D1RA04788D.
22. Prasad, A.K., Park, J.-Y., Kang, S.-H., and Ahn, K.-S. (2022). Electrochemically co-deposited WO_3-V_2O_5 composites for electrochromic energy storage applications. Electrochim. Acta *422*, 140340. https://doi.org/10.1016/j.electacta.2022.140340.
23. Guo, Q., Zhao, X., Li, Z., Wang, D., and Nie, G. (2020). A novel solid-state electrochromic supercapacitor with high energy storage capacity and cycle stability based on poly(5-formylindole)/WO_3 honeycombed porous nanocomposites. Chem. Eng. J. *384*, 123370. https://doi.org/10.1016/j.cej.2019.123370.
24. Yang, J., Lian, L., Ruan, H., Xie, F., and Wei, M. (2014). Nanostructured porous MnO_2 on Ni foam substrate with a high mass loading via a CV electrodeposition route for supercapacitor application. Electrochim. Acta *136*, 189–194. https://doi.org/10.1016/j.electacta.2014.05.074.
25. Wang, K., Gao, S., Du, Z., Yuan, A., Lu, W., and Chen, L. (2016). MnO_2-Carbon nanotube composite for high-areal-density supercapacitors with high rate performance. J. Power Sources *305*, 30–36. https://doi.org/10.1016/j.jpowsour.2015.11.064.
26. Sarkar, D., Mukherjee, S., Pal, S., Sarma, D.D., and Shukla, A. (2018). Hexagonal WO_3 Nanorods as Ambipolar Electrode Material in Asymmetric WO_3//WO_3/MnO_2 Supercapacitor. J. Electrochem. Soc. *165*, 2108–A2114. https://doi.org/10.1149/2.0451810jes.
27. Yang, G., and Liu, X.-X. (2018). Electrochemical fabrication of interconnected tungsten bronze nanosheets for high performance supercapacitor. J. Power Sources *383*, 17–23. https://doi.org/10.1016/j.jpowsour.2018.02.035.
28. Ge, Y., Xie, X., Roscher, J., Holze, R., and Qu, Q. (2020). How to measure and report the capacity of electrochemical double layers, supercapacitors, and their electrode materials. J. Solid State Electrochem. *24*, 3215–3230. https://doi.org/10.1007/s10008-020-04804-x.
29. Xiao, J., Hu, J., Wang, D., Hu, D., Xu, W., Graff, G.L., Nie, Z., Liu, J., and Zhang, J.-G. (2011). Investigation of the rechargeability of Li-O_2 batteries in non-aqueous electrolyte. J. Power Sources *196*, 5674–5678. https://doi.org/10.1016/j.jpowsour.2011.02.060.
30. Freunberger, S.A., Chen, Y., Peng, Z., Griffin, J.M., Hardwick, L.J., Bardé, F., Novák, P., and Bruce, P.G. (2011). Reactions in the Rechargeable Lithium-O_2 Battery with Alkyl Carbonate Electrolytes. J. Am. Chem. Soc. *133*, 8040–8047. https://doi.org/10.1021/ja2021747.
31. Pecquenard, B., Lecacheux, H., Livage, J., and Julien, C. (1998). Orthorhombic WO_3 Formed via a Ti-Stabilized $WO_3 \cdot 13H_2O$ Phase. J. Solid State Chem. *135*, 159–168. https://doi.org/10.1006/jssc.1997.7618.
32. Song, W., Zhang, R., Bai, X., Jia, Q., and Ji, H. (2020). Exposed crystal facets of WO_3 nanosheets by phase control on NO_2-sensing performance. J. Mater. Sci. Mater. Electron. *31*, 610–620. https://doi.org/10.1007/s10854-019-02565-6.
33. Seguin, L., Figlarz, M., Cavagnat, R., and Lassègues, J.C. (1995). Infrared and Raman spectra of MoO_3 molybdenum trioxides and $MoO_3 \cdot xH_2O$ molybdenum trioxide hydrates. Spectrochim. Acta Mol. Biomol. Spectrosc. *51*, 1323–1344. https://doi.org/10.1016/0584-8539(94)00247-9.
34. Pinheiro, D., Pineiro, M., and de Melo, J.S.S. (2021). Sulfonated tryptanthrin anolyte increases performance in pH neutral aqueous redox flow batteries. Commun. Chem. *4*. 89-10. https://doi.org/10.1038/s42004-021-00523-0.
35. Hu, L., Jin, M., Zhang, Z., Chen, H., Boorboor Ajdari, F., and Song, J. (2022). Interface-Adaptive Binder Enabled by Supramolecular Interactions for High-Capacity Si/C Composite Anodes in Lithium-Ion Batteries. Adv. Funct. Mater. *32*, 2111560. https://doi.org/10.1002/adfm.202111560.
36. Bard, A.J., and Faulkner, L.R. (2000). Electrochemical Methods: Fundamentals and Applications (John Wiley & Sons, Ltd).
37. Buss, F., Göcke, J., Scharfer, P., and Schabel, W. (2015). From Micro to Nano Thin Polymer Layers: Thickness and Concentration Dependence of Sorption and the Solvent Diffusion Coefficient. Macromolecules *48*, 8285–8293. https://doi.org/10.1021/acs.macromol.5b01648.
38. Lindström, H., Södergren, S., Solbrand, A., Rensmo, H., Hjelm, J., Hagfeldt, A., and Lindquist, S.-E. (1997). Li^+ Ion Insertion in TiO_2 (Anatase). 2. Voltammetry on Nanoporous Films. J. Phys. Chem. B *101*, 7717–7722. https://doi.org/10.1021/jp970490q.
39. Zhu, M., Meng, W., Huang, Y., Huang, Y., and Zhi, C. (2014). Proton-Insertion-Enhanced Pseudocapacitance Based on the Assembly Structure of Tungsten Oxide. ACS Appl. Mater. Interfaces *6*, 18901–18910. https://doi.org/10.1021/am504756u.
40. Jia, J., Liu, X., Mi, R., Liu, N., Xiong, Z., Yuan, L., Wang, C., Sheng, G., Cao, L., Zhou, X., and Liu, X. (2018). Self-assembled pancake-like hexagonal tungsten oxide with ordered mesopores for supercapacitors. J. Mater. Chem. A *6*, 15330–15339. https://doi.org/10.1039/C8TA05292A.
41. Pan, J., Zheng, R., Wang, Y., Ye, X., Wan, Z., Jia, C., Weng, X., Xie, J., and Deng, L. (2020). A high-performance electrochromic device assembled with hexagonal WO_3 and NiO/PB composite nanosheet electrodes towards energy storage smart window. Sol. Energy Mater. Sol. Cells *207*, 110337. https://doi.org/10.1016/j.solmat.2019.110337.
42. Liu, Z., Fu, D., Liu, F., Han, G., Liu, C., Chang, Y., Xiao, Y., Li, M., and Li, S. (2014). Mesoporous carbon nanofibers with large cage-like pores activated by tin dioxide and their use in supercapacitor and catalyst support. Carbon *70*, 295–307. https://doi.org/10.1016/j.carbon.2014.01.011.
43. Mujawar, S.H., Ambade, S.B., Battumur, T., Ambade, R.B., and Lee, S.-H. (2011). Electropolymerization of polyaniline on titanium oxide nanotubes for supercapacitor application. Electrochim. Acta *56*, 4462–4466. https://doi.org/10.1016/j.electacta.2011.02.043.
44. Bi, Z., Li, X., Chen, Y., Xu, X., Zhang, S., and Zhu, Q. (2017). Bi-functional flexible electrodes

Please cite this article in press as: Wei et al., Boosting areal capacitance in WO_3-based supercapacitor materials by stacking nanoporous composite films, Cell Reports Physical Science (2024), https://doi.org/10.1016/j.xcrp.2024.101836

based on tungsten trioxide/zinc oxide nanocomposites for electrochromic and energy storage applications. Electrochim. Acta *227*, 61–68. https://doi.org/10.1016/j.electacta.2017.01.003.

45. Wang, Y., Shen, G., Tang, T., Zeng, J., Sagar, R.U.R., Qi, X., and Liang, T. (2022). Construction of doped-rare earth (Ce, Eu, Sm, Gd) WO_3 porous nanofilm for superior electrochromic and energy storage windows. Electrochim. Acta *412*, 140099. https://doi.org/10.1016/j.electacta.2022.140099.

46. Li, W., Zhang, J., Zheng, Y., and Cui, Y. (2022). High performance electrochromic energy storage devices based on Mo-doped crystalline/amorphous WO_3 core-shell structures. Sol. Energy Mater. Sol. Cells *235*, 111488. https://doi.org/10.1016/j.solmat.2021.111488.

47. Xie, S., Bi, Z., Chen, Y., He, X., Guo, X., Gao, X., and Li, X. (2018). Electrodeposited Mo-doped WO_3 film with large optical modulation and high areal capacitance toward electrochromic energy-storage applications. Appl. Surf. Sci. *459*, 774–781. https://doi.org/10.1016/j.apsusc.2018.08.045.

48. Cai, G., Darmawan, P., Cheng, X., and Lee, P.S. (2017). Inkjet Printed Large Area Multifunctional Smart Windows. Adv. Energy Mater. *7*, 1602598. https://doi.org/10.1002/aenm.201602598.

49. Lee, S., Lee, Y.-W., Kwak, D.-H., Kim, M.-C., Lee, J.-Y., Kim, D.-M., and Park, K.-W. (2015). Improved pseudocapacitive performance of well-defined WO_{3-x} nanoplates. Ceram. Int. *41*, 4989–4995. https://doi.org/10.1016/j.ceramint.2014.12.064.

50. Li, X., Xiang, L., Xie, X., Zhang, C., Liu, S., Li, Z., and Shen, J. (2020). Effects of electrode thickness and crystal water on pseudocapacitive performance of layered birnessite MnO_2. Nanotechnology *31*, 215406. https://doi.org/10.1088/1361-6528/ab73bf.

51. Gogotsi, Y., and Simon, P. (2011). True Performance Metrics in Electrochemical Energy Storage. Science *334*, 917–918. https://doi.org/10.1126/science.1213003.

52. Stoller, M.D., and Ruoff, R.S. (2010). Best practice methods for determining an electrode material's performance for ultracapacitors. Energy Environ. Sci. *3*, 1294–1301. https://doi.org/10.1039/C0EE00074D.

53. Qi, H., Yick, S., Francis, O., Murdock, A., van der Laan, T., Ostrikov, K.K., Bo, Z., Han, Z., and Bendavid, A. (2020). Nanohybrid TiN/Vertical graphene for high-performance supercapacitor applications. Energy Storage Mater. *26*, 138–146. https://doi.org/10.1016/j.ensm.2019.12.040.

54. Wang, J., Wu, C., Wu, P., Li, X., Zhang, M., and Zhu, J. (2017). Polypyrrole capacitance characteristics with different doping ions and thicknesses. Phys. Chem. Chem. Phys. *19*, 21165–21173. https://doi.org/10.1039/C7CP02707A.